Evaluation of near-field electromagnetic shielding effectiveness at low frequencies

Arellano, Y., Hunt, A. & Haas, O.

Original citation & hyperlink:
Arellano, Y, Hunt, A & Haas, O 2019, 'Evaluation of near-field electromagnetic shielding effectiveness at low frequencies' IEEE Sensors Journal, vol. 19, no. 1, 18320962, pp. 121 - 128.
https://dx.doi.org/10.1109/JSEN.2018.2873909

DOI 10.1109/JSEN.2018.2873909
ESSN 1530-437X

Publisher: Institute of Electrical and Electronics Engineers (IEEE)

Evaluation of near-field electromagnetic shielding effectiveness at low frequencies

Yessica Arellano, Andrew Hunt, and Olivier Haas

***Abstract*—Magnetic Induction Tomography (MIT) is a novel technology for flow measurement offering significant promise in the measurement of multiphase flows containing low-conductivity fluids such as saline water. Such measurements rely on optimal effective shielding to avoid external field interference and extraneous capacitive coupling that can lead to false readings and overestimations of the eddy current induced fields. The performance of various attenuation materials in the low Megahertz frequency spectrum is presented and compared to outcomes from a numerical computational method. The results demonstrate that the shielding mechanism that prevails at low frequencies is that of reflection. Consequently, hard shields such as metals show superior wave attenuation performance for MIT systems operating below 13 MHz. For higher frequencies, the absorption effect on the incident wave path within soft electromagnetic shields presents enhanced shielding properties. This paper also explores the limitations of traditional testing geometry for shielding effectiveness and proposes an alternative approach to near-field, free-space measurement for MIT sensors. The proposed semi-enclosed approach shows enhanced shielding effectiveness measurements compared to the traditional transversal barrier method. The proposed method was used to assess the electromagnetic shielding effectiveness of ferromagnetic and various metallic materials.**

***Index Terms*— Eddy Currents, Electromagnetic Compatibility, Electromagnetic Induction, Electromagnetic Shielding, Tomography.**

I. Introduction

MAGNETIC Induction Tomography (MIT) is an imaging technology based on electromagnetic field induction. The principle of operation is the energisation of a sensor array with a sinusoidal alternating current that generates a magnetic field. This alternating magnetic field induces a voltage in the receiving sensors, following Faraday's Law. The induced signal received by the sensing coils is directly proportional to the strength of the primary magnetic field. If an electrically conductive object is placed within the magnetic field, eddy currents are induced in the object, disturbing the primary field distribution and producing a secondary magnetic field [1]. The resultant field perturbations are measured by an array of detection coils located around the perimeter of a pipe. The electromagnetic property distribution of a conductive phase is inferred from the measurements obtained by the sensor array [2].

The accuracy of MIT devices is closely related to the insulation of the system from external field interference, and to the elimination of capacitive coupling among sensors. Reportedly, capacitive coupling and noise induced by improperly screened instrumentation greatly affect the system readings, resulting in an overestimation of the secondary field of up to 70% [3], [4]. Accordingly, electromagnetic shielding of these systems is necessary to confine the electromagnetic field, avoid interference from external sources, and create a path for electrical coupling to the ground, as demonstrated by a number of works in the literature [5], [6]. Furthermore, capacitive coupling due to electric field attraction for low conductive environments is significantly reduced by installing external electromagnetic enclosures that act as a ground plane [7]. Typically, MIT systems for low conductivity measurement operate within the low MHz range, below 20 MHz [8]. This frequency range ensures wavelengths larger than the characteristic dimensions of the region of interest (ROI) [9]. Low conductivity imaging through MIT relies on conductive materials for electromagnetic shielding [5], [10], [11], [12], [13]–known as hard shields. Traditionally, the use of packed ferromagnetic material as soft shields, alone or combined with conductive shields, has been limited to imaging of highly conductive materials within the low kHz frequency spectrum [1], [14], [15], [6]. There is, therefore, an opportunity to investigate the applicability of soft shields for MIT systems operating in the low MHz spectrum. There is also an opportunity to extend the results of [5] and [6] on the effect that geometric parameters have on the performance of MIT shields.

Electromagnetic interference shielding consists of a physical barrier that prevents time-varying electromagnetic fields to radiate from or into the ROI. The widely accepted theory on electromagnetic shielding was initially derived from [16]. It states that the shielding effectiveness (SE) of a material is the combination of the reflected losses at the outer and inner walls, and the absorption and multiple reflection losses within the material body. The penetration of the electromagnetic radiation in a shield drops exponentially with increasing depth into the material. Particularly, within the low MHz frequency range, electrometric radiation penetrates only the near-surface region of the shield, given by the skin depth [17].

The effectiveness of a shield to block an incident magnetic field depends on the dielectric properties of the material barrier, i.e., the complex, relative permeability (μ_r) and permittivity (ε_r)

978-1-5386-5541-2/18/$31.00 ©2018 IEEE

[18]. It is also influenced by the operating frequency, the location of the field in regards to the wavelength (near or far fields), the continuity of the surface, and the thickness of the shield [19], [20]. Three primary methods have been developed for measurement of complex permeability, namely the transmission/reflection line method, the free space method, and the resonant method [18], [21], [22]. Each methodology is limited to specific materials and applications [23].

This paper combines numerical simulation and experimental testing to evaluate the effectiveness of soft, hard and composite shields for use in MIT systems. It differs from published work in terms of the frequency range studied, the design targeted to MIT sensing systems, and the SE evaluation method. The proposed SE evaluation method, for the first time, partially encloses the receiving sensor with the attenuation material. The results from this novel approach show enhanced accuracy when compared to experimental data collected using the near-field free-space transversal barrier method. Furthermore, the experimental results obtained on various attenuation materials and geometries can be exploited in the design of new shielding materials.

The experimental outputs were analysed through a combination of statistical techniques. Statistical analysis was performed on the experimental data to assess the quality of the measurements and to help understand the relationship of a broad range of parameters. The probability distribution and dispersion of the experimental data were calculated through mean and standard deviation measures. The confidence interval (CI) gives the probability that the measurements lie within a particular distance from the mean value [24]. In this work, the 95% CI was adopted. Through the Analysis of Variance (ANOVA), means of data measured from several attenuation materials were critically evaluated [25]. The Welch test was used for means comparison in cases where variances were different. Finally, the post-hoc tests provided a measure of the results statistical significance for the shielding materials investigated.

II. Electromagnetic Shielding

Electromagnetic shielding is characterised by reflection, absorption and multiple-reflection mechanisms. In cases where the absorption loss is higher than 10 dB, most of the inner reflected signal is absorbed within the material [26]. Accordingly, the effect of multiple reflections can be neglected for shield thicknesses larger than the skin depth [4]. Consequently, the primary mechanisms for near magnetic fields, as in MIT, are absorption and reflection losses. The absorption loss mechanism is related to the exponential decrease in amplitude of the wave as it passes through a medium due to Ohmic losses and material heating [27]. Hence, materials with electric or magnetic dipoles and high magnetic permeability provide high absorption shielding efficiency [28]. Conversely, reflective loss is based on radiation reflection of barriers that tend to be composed by metallic materials due to their conductivity and capacity for charge mobility.

Penetration of the shields can arise from both the electric and the magnetic components of the electromagnetic energy interacting with the attenuation materials. However, within the low range of frequencies (50 Hz to 20 MHz), the form of expressing SE in dB, denoted as S_H, is solely related to the magnetic field performance [29], given by:

$$S_H = 20 \log_{10} \frac{H_i}{H_t} \quad (1)$$

where H_i is the magnetic field in the absence of the attenuation material and H_t is the magnetic field with the shield positioned between the magnetic sensors.

Note that the result from Equation (1) yields a positive value since the incident field is expected to be higher than the transmitted field. Alternatively, SE can be defined in terms of the rate of the transmitted field to the incident field [17]. Nevertheless, within this work, the SE is regarded as an insertion loss equivalent to the ratio of the magnetic field with the shield removed to that incident on the barrier when the shield is in place.

Quantification of the attenuation of an incident wave when in contact with a barrier is achieved by measuring the material SE. The incident magnetic field or *reference measurement* is the background signal detected by the MIT sensor in the absence of the shielding material. The attenuated wave measured by the receiving sensor is equivalent to the signal transmitted through the surface of the shielding barrier [30]. For electromotive force (emf) measurements in the time domain, Equation (1) is equivalent to Equation (2) [8] with the SE in dB, denoted as S_H, given by:

$$S_H = 20 \log_{10} \frac{V_1}{V_2} \quad (2)$$

where V_1 is the reference voltage on the receiving coil, without the barrier and V_2 is the voltage reading with the shielding material in place, referred to as the *load measurement*.

The use of a free-space measurement method that uses electromagnetic probes for near-field region measurement is the best approach to emulate the operating features of MIT systems. The experimental setup reported here was designed to account for a near-field magnetic measurement with a distance between sensors of at least two orders of magnitude smaller than the wavelength (λ). This design is in concordance with the inductive near-field behaviour of electromagnetic fields that dominate the vicinity of the excitation source within a distance no greater than $\lambda/2\pi$.

The evaluation procedure consists of the measurement of the SE of various attenuation materials located between two circular loop coils, commonly used as MIT sensors. By comparing the acquired signal to the reference voltage, the SE can be determined using Equation (2).

III. METHODOLOGY

The methodology adopted to evaluate the SE of a range of attenuation materials with varying mechanical and electrical properties comprises the following stages:

– Prepare samples with different materials and thicknesses (an assortment of attenuation materials that are of interest or have been used in existing MIT systems was selected).

– Setup the experiments using MIT sensors with three configurations namely: without shielding, with a standard shield configuration and with the proposed shielding configuration.

– Perform numerical simulation to visualise the impact of the different settings on the electromagnetic field distribution.

– Perform the measurements under controlled conditions.

– Analyse the measurement qualitatively and quantitatively using statistics.

The following subsections describe the experimental setup and the computational approach used to solve the electromagnetic problem numerically.

A. Sample Materials

The evaluated attenuation materials account for hard and soft shields, from samples of metals and dust-state ferrite, respectively. The electrical properties of the metals are summarised in TABLE I. Seven samples, labelled Al6, Al2, MS, MM, FP20, FP5, and MF5, were prepared (See TABLE II). Al6 and Al2 samples are Aluminium sheets with thicknesses of 6.3 mm and 2.1 mm, respectively. MS is a 2.1 mm Mild Steel sample. MM is a Mu-Metal alloy sheet with a thickness of 0.1 mm. Perspex pockets with bulk dimensions of 20 mm and 5 mm filled with Ferrite Powder were labelled FP20 and FP5, respectively. Finally, a combination of Mu-Metal (0.1 mm) and Ferrite Powder (5 mm) forming a dual shielding assembly (MF5) was prepared for further shielding capability testing. All samples used were sized to 120 mm × 130 mm to account for standard surface dimensions and allow a direct comparison of their performances.

TABLE I
ELECTRICAL PROPERTIES OF SHIELDING MATERIALS

Material	Relative Conductivity (σ_r)	Relative Permeability (μ_r)	Reflective Loss (σ_r/μ_r)	Absorption Loss ($\sigma_r\mu_r$)
Aluminum	5.87×10^{-1}	1	5.87×10^{-1}	5.87×10^{-1}
Mild Steel	1.17×10^{-1}	1.0×10^{2}	1.17×10^{-3}	1.17×10^{1}
Mu-Metal	2.80×10^{-2}	90×10^{3}	3.11×10^{-7}	2.52×10^{3}
Ferrite Powder	1.68×10^{-1}	N/A	-	-

NOTE–Relative properties computed using data of Copper, Aluminum and Mild Steel from [31], Mu-Metal from [32], and Ferrite from [33].

TABLE II
SAMPLE CODING FOR ATTENUATION MATERIALS

Code of Material	Name of Material	Thickness of Shield (t)	Ratio[a] $\left(\frac{t}{\delta}\right)$	Type of Shield
Al6	Aluminium	6.3 mm	165	Hard
Al2	Aluminium	2.1 mm	55	Hard
MS	Mild-Steel	2.1 mm	247	Hard
MM	Mu-Metal	0.1 mm	172	Hard
FP20	Ferrite Powder	20.0 mm	1257	Soft
FP5	Ferrite Powder	5.0 mm	314	Soft
MF5	Mu-Metal & Ferrite Powder	5.1 mm	172	Composite

[a]Ratio of barrier thickness to material skin depth at 10 MHz

B. Experimental Setup

The experimental SE evaluation for pipeline imaging through MIT considers driving frequencies between 5 MHz and 20 MHz. The frequency range ensures that the sensors operate within the electromagnetic near zone. This near-zone, which covers a distance much greater than the dimensions of the experimental system, is limited to 2.3 m from the electromagnetic source for the particular frequency spectrum of interest.

The incident and transmitted fields were measured using the experimental setup illustrated in Fig. 1. The experimental assembly is equivalent to a dual coil MIT system, with the MIT sensors used as electromagnetic probes. The transmitting coil (Tx) is excited via a function generator (GW Instek AFG-2125). The excitation signal in form of a sine wave induces a magnetic field that is sensed by the receiving coil (Rx). Rx, located at 180^0 from Tx, is connected to a digital oscilloscope (PicoScope 5444B) for measurement of the magnetic field that permeates the shielding material. A fixed distance, equal to the coils diameter, separates the coils and the attenuation material to ensure a dimension-to-distance ratio as specified in [8].

The source coil was excited with a peak-to-peak potential difference of 10 V. All metallic samples were grounded to ensure electrical coupling to ground and avoid false readings due to capacitive coupling. Circular helix air-core coils with six turns and 50 mm inner diameter were used. Coils were wound in the same direction, and their terminals were connected so that the mutual flux linkage of the transmitting and receiving coil adds to the self-inductance of the receiving coil following the right-hand-side rule [34].

Reference and load measurements were repeatedly taken throughout the frequency spectrum. The reference readings were measured without the shielding material between the sensors, see Fig. 1a. Following the measurement procedure in [8], the load measurements were gathered with the attenuation material placed equidistantly between the sensors and orthogonally to the incident wave. The edges of the shields were equidistant from the sensors. This configuration provides experimental rigour as the angle of the incident wave is kept fixed for all measurements. The incident angle defines the path of the transmitting signal across the material cross-section, and hence affects the absorption losses within the barrier body.

Fig. 1b and Fig. 1c illustrate the experimental setup for a near-field magnetic SE measurement in free space [35], [36]. The experimental setup presented in Fig. 1d constitutes a novel approach to the traditional near-field transversal barrier SE measurement method in Fig. 1b. The proposed Rx semi-enclosed method in Fig. 1e uses a uniform circular shield of 275 mm diameter to encapsulate Rx. The design and dimensions of the enveloping shield are typical in MIT systems where the ROI is defined by multiphase pipeline diameters. In MIT systems for flow measurement, the shield radially encloses the sensor array, which is located around the pipe perimeter. Changing the typical MIT assembly by placing the shield between the sensors allows its SE to be assessed. For both valuation methods in

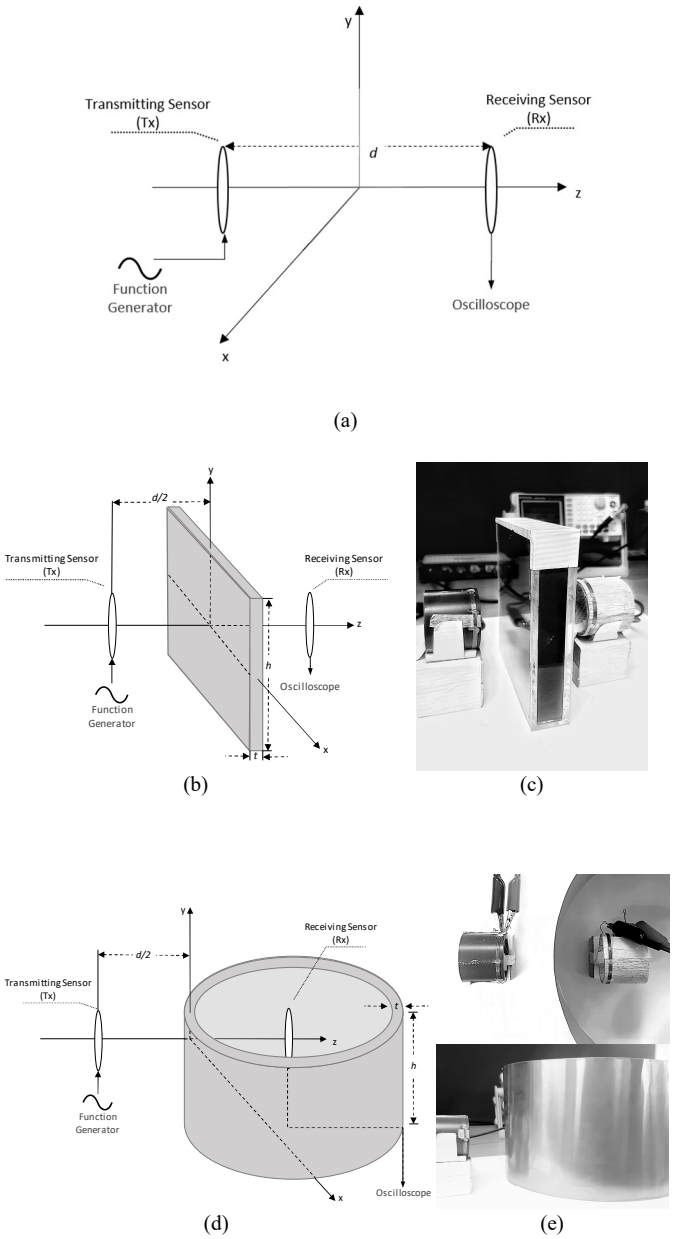

Fig. 1. Experimental setup for SE tests of the attenuation materials between MIT-type of sensors. (a) Base case: reference measurement without shielding barrier. (b) 3D diagram of the load measurement from the near-field transversal barrier measurement method with a shielding material positioned between the sensors. (c) Picture of a transversal barrier setup (FP20) used during experiments. (d) Diagram of load measurement for the proposed configuration of near-field magnetic measurement method from a partially enclosed receiving sensor. (e) Top and side views of the receiving coil partially enclosed in a cylindrical shield.

Fig. 1b and Fig. 1d, the SE is calculated from the ratio of the emf induced, using Equation (2).

For the base case and every attenuation material, 32000 samples were gathered at a sampling rate of 250 MS/s. The size of the collected data is over 4 Gigasamples for all measurements at frequencies 5 MHz to 20 MHz. Experiments were conducted at room temperature.

C. Numerical Simulation

Computational modelling of the electromagnetic fields is based on numerically solving Maxwell's equations using finite element method. The model presented in this paper was created using the computer software CST Microwave Studio, Student Edition. The sensors geometry was modelled using stranded conductors enclosed in dummy torus to improve mesh quality in the area of interest. The shielding barriers thickness and materials varied according to the requirements of each set of experiments. The numerical simulations consider vacuum conditions and insulated environments that disregard the electromagnetic noise and the interference of external sources to which free-space sensors are subjected. The numerical results obtained are hence an ideal representation of the physical phenomena measured with the experimental setup.

Model validation was carried out by evaluating the performance of the model under conditions with readily known responses. In this sense, validation comprised: inclusion of a metallic barrier of known properties between the sensors, change in the dielectric properties of the material, change in the operating frequency and change in the dimensions of the barrier.

Three scenarios were modelled. The first involved the visualization of the effect that varying the thickness of aluminium barriers has on the electromagnetic shielding at various frequencies. The second scenario accounted for the evaluation of the attenuation material using the proposed semi-enclosed Rx evaluation method. In this model, Rx is isolated from the primary magnetic field by a shielding surface with no lateral edges. Finally, a comparison between the performances of both evaluation methods at varying shield heights was made.

D. Statistical analysis of outputs

Statistical analysis of the experimental data is based on the common assumption of normally distributed samples and random sampling of data. Dispersion of the data was measured through the standard deviation for every set of data, each accounting for 32000 emf measurements. The mean emf values for all materials are used to calculate the SE at given frequencies using Equation (2). The mean SE from all seven materials are analysed following the procedure shown in Fig. 2. The results from the test of homogeneity of variances define the method to use for means comparison (ANOVA or Welch). Further post-hoc tests determine the significance of the variance between the evaluated materials.

IV. Results and Discussion

The mean electromagnetic SE of the sample materials for the frequency range 5MHz to 20 MHz computed from experimental data is presented in Fig. 3. The total standard deviation (SD) of the measured emf is 3.05 mV and that of the SE is 0.41 dB. The 95% confidence interval of the mean SE of all attenuation materials is represented as error bars in Fig. 3. Dismissing the equality variance hypothesis (probability value $p < 0.05$), results show that there is a significant difference among materials as determined by Welch (p=0.003).

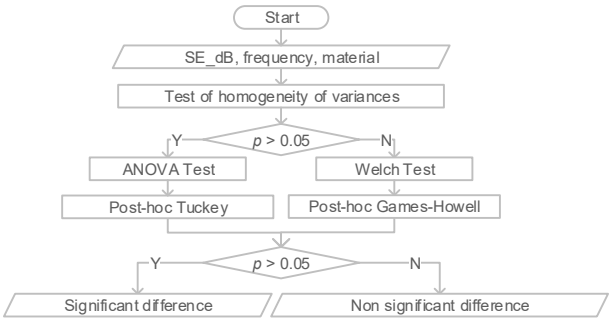

Fig. 2. Statistical procedure for significant difference analysis of SE results from 7 material samples

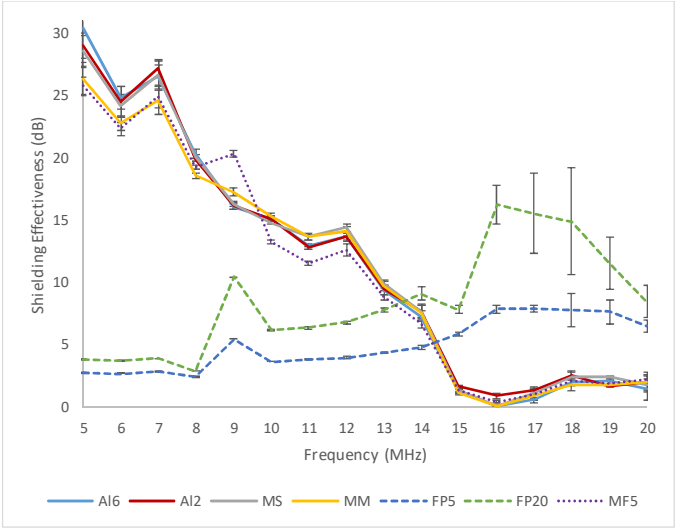

Fig. 3. Experimental results of SE of sample materials in the 5-20 MHz range showing error bars for the 95% Confidence Interval.

Consecutive secluded analyses for hard and soft shields were performed. Games-Howell post-hoc tests revealed that the SE of FP20 (8.33±4.4, p=0.013) was statistically significantly higher compared to that of FP5 (4.98±2.08). There was, however, no statistically significant difference between the hard attenuation materials (F=0.012, p=0.998).

The SE of solid metallic barriers was found to decrease with increasing frequency. There was minimal variation regarding the layer thickness in concordance with typical reflection loss behaviour of metals [28]. Conversely, the inclusion of soft shields built from ferrite powder samples resulted in increased electromagnetic shielding capacity. This increase was correlated with frequency and barrier thickness.

Within the 5-8 MHz frequency range, the aluminium samples (Al6 & Al2) provide the highest attenuation with 23.6 dB on average. Mu-Metal shields show a slightly better performance for shielding the electromagnetic waves within the 9-13 MHz range. Above 13 MHz, Ferrite Powder samples (FP20 & FP5) surpass the performance of hard shields reaching maximum effectiveness of 16 dB (FP20) at 16 MHz, whereas the shielding capacity of metallic samples is nearly null.

Based on results from [6], the composite shielding sample (MF5) was expected to provide enhanced shielding properties by combining hard and soft shields materials. However, it exhibited a similar SE to that of the MM sample, regardless of the relative position of the compounds layers. This behaviour suggests the generation of a low reluctance path of the transmitted signal in the soft shield, which results in a higher concentration of the transmitted electromagnetic field and hence a lower SE.

The responses obtained from the validation tests performed on the simulation model resulted in a decrease of several orders of magnitude of the electromagnetic field on the side of the shielding material opposite to Tx. Fig. 4a illustrates the blocking effect in the magnetic field distribution of a Mu-metal screen of 0.1 mm located between Tx (left) and Rx (right) at an operating frequency of 10 MHz. In addition, changes in the induced emf and in the distribution of the magnetic field were seen with changing dielectric properties, operating conditions, and barrier dimensions. All the above changes are consistent with the laws of physics. Furthermore the outputs from numerical simulations and the responses of the system during experimental tests are in agreement, e.g. Fig. 3 and Fig. 5.

The numerical results of the near-field system at a distance of 15 mm from the shield, for various aluminium barrier thicknesses, is shown in Fig. 5. Similarly to Fig. 3, the results in Fig. 5 evidence a narrow difference in the intensity of the magnetic field close to the receiving sensor with varying barrier thicknesses. This slight difference becomes even less significant with increasing frequency. Experimental and numerical outputs provided the evidence that the SE with varying barrier thicknesses of hard shield differs marginally. In the case of soft shields, experimental results show that varying the barrier thickness has a significant impact on the SE at larger frequencies, e.g., above 13 MHz, see Fig. 3.

Fig. 4 illustrates the magnetic field distribution around Rx for both experimental approaches: transversal barrier method (left) and partial enclosure (right). The electromagnetic simulations indicate the generation of a fringe effect near the borders of the transversal barrier (Fig. 4a and Fig. 4b). To overcome this effect, larger shields are required. The proposed experimental method does not restrict the shielding material to a transversal barrier between the coils. Instead, it partially encloses Rx, increasing the surface of the barrier surface in the XZ direction, yet maintaining the same barrier height (Y plane) and thickness. Numerical outputs result in a 50% decrease in the electromagnetic field distribution inside the enclosure. The partial-enclosure method also reduces the fringe effect on the edges of the shield by more than 47% compared to using the standard transversal barrier. Such effect is attributed to the increase in the surface area of the shield. This results in an enlargement of space available for the magnetic flux to circulate around the shield section, defined by the skin depth, consequently decreasing the reluctance of this path. The geometry of the partial enclosure, however, has the drawback of being more complex resulting in longer experimental preparation time.

The dimensions of the shielding barriers affect the SE

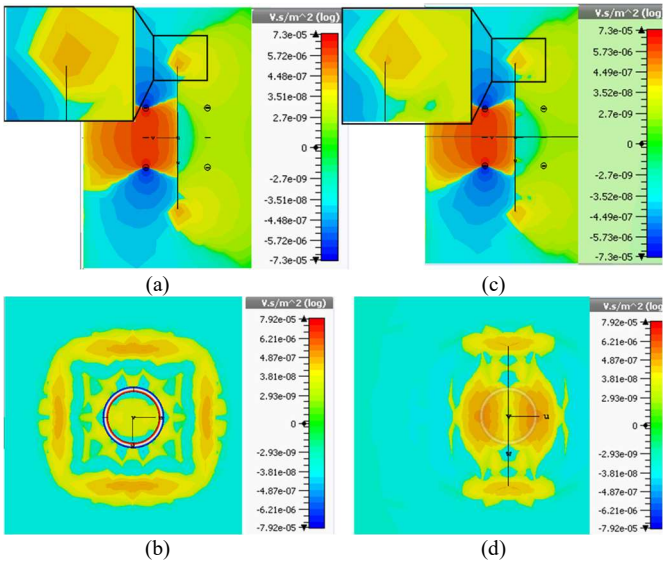

Fig. 4. Magnetic field distribution around Tx and shield at 10 MHz. Top row shows the side view (YZ plane–see Fig. 1) of the model and the bottom row shows the front view (XY plane–see Fig. 1). Images (a) and (b) represent a standard near-field transversal barrier measurement setup using an MM screen. (c) and (d) show the model of a Mu-Metal shield partial enclosing the receiving sensor.

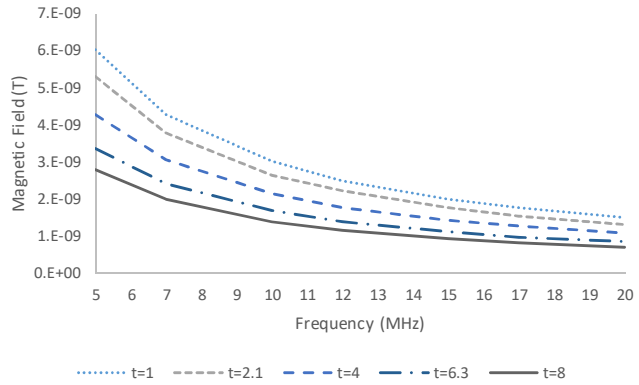

Fig. 5. Numerical results on the effect that varying the thickness of an aluminium barrier has on the transmitted magnetic field intensity at a distance of 15 mm from the barrier wall for relevant frequencies for magnetic induction tomography.

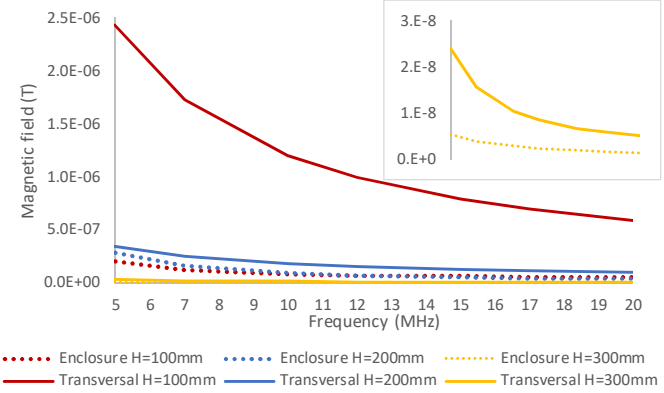

Fig. 6. Numerical results showing the effect that varying the height of Mu-metal barrier has on the magnetic field intensity at the top of the shield (fringe effect). The continuous lines correspond to an assembly like in the transversal barrier method. The dotted curves represent the partial enclosure setup.

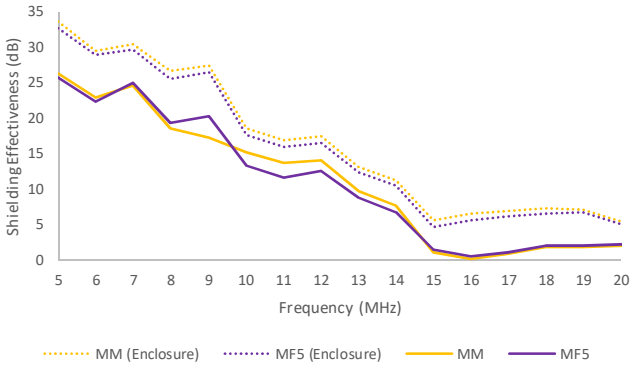

Fig. 7. Experimental results of SE of sample materials in the 5-20 MHz range showing the signal attenuation of MM and MF5 samples at two experimental setups. The continuous lines correspond to samples positioned according to the near-field transversal barrier measurement method. The dotted curves represent the results from the proposed configuration of near-field magnetic measurement method with a partial enclosure of the receiving sensor.

measurements. Fig. 6 shows the electromagnetic field intensity measured at the top of the shield for barrier heights of 100 mm, 200 mm and 300 mm. The partial-enclosure method systematically provided greater field attenuation because of the reduced fringe effect. For the experimental setup used in this paper, a shield height-to-coil diameter ratio of 6 avoided the formation of a fringe field at the top of the barriers. In agreement with [5], this resulted in a more efficient shield performance, and consequently, a more precise SE estimation. Care is advised in extrapolating this results, as different geometric parameters and field distributions would require specific analysis. Furthermore, reduction of the enclosure diameter could potentially lead to internal reflections between the walls of the attenuation material, and hence an underestimation of the material SE.

Complementing the numerical model, experimental results presented in Fig. 7 compare the SE of MM sample with that of a Mu-Metal enclosure. Results show an average increase of 5 dB in SE of both Mu-Metal and MF using the proposed Rx semi-enclosed experimental method. The enhanced SE measurement of the partial enclosure is attributed to the decrease of the fringe effect at the shield edge. This results in a lower intensity of the electromagnetic field inside the enclosure as supported by the simulation results. The significance of this result is that, at an operating frequency of, for example, 9 MHz the blocked field would increase from 96.5% to 99.6%.

V. Conclusions

The shielding effectiveness (SE) of four attenuation materials and one composite (Aluminium, Mild Steel, Mu-Metal, Ferrite, Ferrite/Mu-Metal) was evaluated using two experimental configurations. The SE of hard shields was found to decrease with increasing frequency, regardless of the material or barrier thickness. Conversely, soft shields, which rely primarily on absorption loss mechanisms, are highly dependent on their bulk dimension. They have the advantage of providing an improved attenuation capacity at higher

frequencies. The results presented in this paper are critical in designing shields for MIT systems, as the effects on material selection and shield dimensioning are particularly significant at frequencies typical of MIT systems for low-conductivity samples. Hard shields have a superior wave attenuation performance for MIT systems operating below 13 MHz. For higher frequencies, the absorption effect on the incident wave path within a soft electromagnetic shield presents enhanced shielding properties.

The numerical simulations indicate that the dimensions of the material barriers have a significant impact on the load measurement accuracy of near-field, free-space methods. A proposed semi-enclosed Rx measurement method provides a more accurate representation of the material isolation properties as the load measurement is corrected by eliminating the fringe effect at the side boundaries of the barrier. Moreover, the semi-enclosed method proved to decrease the intensity of the fringe effect at the top and bottom of the barrier, for an enclosure of equal height than the transversal screen. By eliminating the influence of at least one of the dimensional variables, the proposed method leads to a better approximation of the behaviour of the material for final geometrical arrangements of MIT shields.

REFERENCES

[1] H. Griffiths, "Magnetic induction tomography," in *Electrical Impedance Tomography*, D. Holder, Ed. London: IOP Publishing Ltd., 2005.

[2] L. Ma, D. Mccann, and A. Hunt, "Combining Magnetic Induction Tomography and Electromagnetic Velocity Tomography for Water Continuous Multiphase Flows," *IEEE Sens. J.*, vol. 17, no. 24, pp. 8271–8281, 2017.

[3] H. Wei and A. Wilkinson, "Design of a sensor coil and measurement electronics for magnetic induction tomography," *IEEE Trans. Instrum. Meas.*, vol. 60, no. 12, pp. 3853–3859, 2011.

[4] H. Griffits, W. R. Stewart, and W. Gough, "Magnetic Induction Tomography A measuring System for Biological Tissues." Annals New York Academy of Sciences, 1999.

[5] A. J. Peyton, S. Watson, R. J. Williams, H. Griffiths, and W. Gough, "Characterising the effects of the external electromagnetic shield on a magnetic induction tomography sensor.," *3rd World Congr. Ind. Process Tomogr.*, pp. 1–6, 2003.

[6] Z. Yu, P. Worthington, S. Stone, and A. Peyton, "Electromagnetic screening of inductive tomographiuc sensor," in *Proc. ECAPT*, 1995, pp. 300–310.

[7] H. Griffiths, W. Gough, S. Watson, and R. J. Williams, "Residual capacitive coupling and the measurement of permittivity in magnetic induction tomography.," *Physiol. Meas.*, vol. 28, no. 7, pp. S301–S311, 2007.

[8] IEEE Standards Committee, "IEEE Standard Method for Measuring the Effectiveness of Electromagnetic Shielding Enclosures," vol. 1997. The Institute of Electrical and Electronics Engineers, Inc., 1997.

[9] A. Peyton, "Mutual inductance tomography," in *Process Tomography: Principles, Techniques and Applications*, R. A. Williams and M. S. Beck, Eds. Oxford: Butterworth Heinemann, 1995, pp. 85–100.

[10] H.-Y. Wei and M. Soleimani, "Hardware and software design for a National Instrument-based magnetic induction tomography system for prospective biomedical applications.," *Physiol. Meas.*, vol. 33, no. 5, pp. 863–79, 2012.

[11] A. Korjenevsky, V. Cherepenin, and S. Sapetsky, "Magnetic induction tomography: experimental realization," *Physiol. Meas.*, vol. 21, no. 1, pp. 89–94, 2000.

[12] S. Watson, R. J. Williams, W. Gough, and H. Griffiths, "A magnetic induction tomography system for samples with conductivities below 10 S/m," *Meas. Sci. Technol.*, vol. 19, no. 1, pp. 1–11, 2008.

[13] H. C. Wee, S. Watson, R. Patz, H. Griffiths, and R. J. Williams, "A magnetic induction tomography system with sub-millidegree phase noise and high long-term phase stability," *IFMBE Proc.*, vol. 22, pp. 744–747, 2008.

[14] A. J. Peyton *et al.*, "An overview of electromagnetic inductance tomography: description of three different systems," *Meas. Sci. & Technol.*, vol. 7, no. 3, pp. 261–271, 1996.

[15] G. M. Lyon, Z. Z. Yu, A. J. Peyton, and M. S. Beck, "Development in electro-magnetic tomography instrumentation," *IEE Colloguium Adv. Electr. Tomogr.*, p. 12/1-12/4, 1996.

[16] S. A. Schelkunoff, *Electromagnetic waves*. Boston: D. Van Nostrand Company, Inc., 1945.

[17] C. Paul, *Introduction to Electromagnetic Compatibility*, Second. John Wiley & Sons, Inc, 2006.

[18] K. C. Yaw, "Measurement of dielectric material properties." Rohde&Schwarz, pp. 1–36, 2012.

[19] L. Jin, Z. Haiyan, L. Ping, Y. Xijiang, and Z. Guoxun, "The electromagnetic shielding effectiveness of a low-cost and transparent stainless steel fiber/silicone resin composite," *IEEE Trans. Electromagn. Compat.*, vol. 56, no. 2, pp. 328–334, 2014.

[20] H. Haus and J. Melcher, *Electromagnetic fields and energy*. Prentice Hall Books, 1989.

[21] V. Voicu, I. P. Ă. Tru, P. Nicolae, S. M. Ieee, and L. Dina, "Analyzing the Attenuation of Electromagnetic Shielding Materials for Frequencies under 1 GHz," in *Advanced Topics in Electrical Engineering (ATEE)*, 2017, pp. 336–339.

[22] C. A. Feickert, M. K. McInerney, and W. . Croisant, "Resonant eddy current analysis: A selective screening method for electromagnetic shielding materials," in *1993 International Symposium on Electromagnetic Compatibility*, 1993, pp. 160–163.

[23] A. Tamburrano, D. Desideri, A. Maschio, and M. S. Sarto, "Coaxial waveguide methods for shielding effectiveness measurement of planar materials up to 18 GHz," *IEEE Trans. Electromagn. Compat.*, vol. 56, no. 6, pp. 1386–1395, 2014.

[24] Graphpad Statistics Software, "GraphPad Statistics Guide," 2017. [Online]. Available: https://www.graphpad.com/guides/prism/7/statistics/stat_confidence_interval_of_a_stand.htm?toc=0&printWindow. [Accessed: 23-Jan-2018].

[25] Universidad de Granada, "Contrastes de hipostesis," 2018. [Online]. Available: http://wpd.ugr.es/~bioestad/guia-spss/practica-6/. [Accessed: 01-Feb-2018].

[26] M. H. Al-saleh, W. H. Saadeh, and U. Sundararaj, "EMI shielding effectiveness of carbon based nanostructured polymeric materials : A comparative study," *Carbon N. Y.*, vol. 60, no. 2, pp. 146–156, 2013.

[27] R. Kotnala and J. Shah, "Chapter 4 - Ferrite Materials: Nano to Spintronics Regime," in *Handbook of Magnetic Materials*, K. Buschow, Ed. Amsterdam: Elseiver, 2015.

[28] D. D. L. Chung, "Materials for Electromagnetic Interference Shielding," *J. Mater. Eng. Perform.*, vol. 9, no. October 1999, pp. 350–354, 2000.

[29] R. Schulz, V. Plantz, and D. Brush, "Shielding Theory and Practice," *IEEE Trans. Electromagn. Compat.*, vol. 30, no. 3, pp. 187–201, 1988.

[30] J. V. Vas and M. J. Thomas, "Electromagnetic shielding effectiveness of layered polymer nanocomposites," *IEEE Trans. Electromagn. Compat.*, vol. 60, no. 2, pp. 376–384, 2018.

[31] D. R. Lide, *CRC Handbook of Chemistry and Physics*. CRC Press LLC, 2005.

[32] ASTM A753-08, "Standard Specification for Wrought Nickel-Iron Soft Magnetic Alloys (UNS K94490, K94840, N14076, N14080)." ASTM Internationa, West Conshohocken, PA, 2013.

[33] W. F. Brown, *Handbook of Chemistry and Physics*. McGraw-Hill, 1958.

[34] F. W. Grover, *Inductance calculations: working formulas and tables*. New York: D. Van Nostrand Co., 1973.

[35] C. Morari and I. Balan, "Methods for determining shielding effectiveness of materials," *Electroteh. Electron. Autom.*, vol. 63, no. 126–136, 2015.

[36] S. Criel, L. Martens, and D. De Zutter, "Theoretical and Experimental Near-Field Characterization of Perforated Shields,"

IEEE Trans. Electromagn. Compat., vol. 36, no. 3, pp. 161–168, 1994.

Yessica Arellano received her BE and M.Sc. degrees from La Universidad del Zulia in 2005 and 2011 respectively. A second M.Sc. with distinction was awarded by the Robert Gordon University in 2008. She is currently pursuing the Ph.D. degree in Flow Measurement and Fluid Mechanics at Coventry University, UK. Since the year 2005, she worked within the Oil and Gas Industry, initially as a member of the facilities department in offshore fields in Venezuela and from 2010 to 2016 as a R&D Engineer in fluid mechanics at INTEVEP S.A. Her current research focuses on multiphase flow metering through tomography techniques.

Andrew Hunt received his BSc degree in Aeronautical Engineering from the University of Bristol (UK) in 1978, and his PhD in aerodynamics from Cranfield University (UK) in 1982. He is Professor of Oil and Gas Engineering at Coventry University, Technical Director at iPhase Ltd, and CEO of Atout Process Ltd, all in the UK. After being post-doctoral research fellow and lecturer at the University of Surrey he spent 15 years in the oil industry with Schlumberger, one of the world's 'big three' oilfield service companies where he was Head of Fluid Dynamics Research and Product Development Director. Andrew Hunt is a Chartered Engineer, Fellow of the Institute of Measurement and Control, and has been visiting professor at the University of Manchester (1996 to 2002) and vice-President of the Institute of Measurement and Control (2002-2007).

Olivier C. L. Haas received his PhD from Coventry University (UK) in 1997. He is reader in Applied Control Systems and member of the Future Cities Research group. He has expertise in multi-objective optimization, control engineering, systems modelling, image processing and artificial neural network. Until recently his main research are was radiotherapy physics. He is currently focusing on intelligent transportation systems and connected vehicle. He is the principal investigator of the innovate UK funded UK Connected Intelligent Transport Environment (UK CITE) and the CW LEP funded Intelligent Variable Message Systems. He is reviewer for EPSRC (UK) and Plan Cancer (Fr). He has authored and co-authored over 150 scientific and technical papers, chapters and books and has successfully supervised 15 PhD students.